Journal of Mathematical Modeling
Vol. -, No. -, 2026, pp. -. Research Article

JMM

A meshfree MLPG strategy for phase-field fracture analysis utilizing RPIM interpolants

Amin Abrishami Moghadam, Ali R. Soheili*

Department of Applied Mathematics, Faculty of Mathematical Sciences, Ferdowsi University of Mashhad, P.O. Box 1159, Mashhad 91775, Iran

Email(s): amin_abrishamimoghadam@mail.um.ac.ir, soheili@um.ac.ir

Abstract. A meshfree numerical scheme is developed here to investigate fracture processes using elasticity-based principles. By synthesizing energy functionals for damage growth with linear elastic theory, the governing Euler–Lagrange equations for a phase-field fracture (PFF) environment are derived. To bypass the topological constraints of mesh-based techniques, the Meshless Local Petrov–Galerkin (MLPG) architecture is employed. A significant feature of this work is the integration of Radial Point Interpolation Method (RPIM) functions; these interpolants inherently possess the Kronecker delta property, which streamlines the imposition of Dirichlet boundary conditions. The field approximation and nodal connectivity are meshfree; Cartesian background cells are used solely for numerical integration and do not constitute a field-approximation mesh or global element connectivity. The manuscript details the spectral splitting of the strain tensor (Miehe-type tensile/compressive split) and provides the semilinear weak forms required for a staggered iteration algorithm. The robustness of the proposed meshless model is showcased through various 2D fracture benchmarks.

Keywords: MLPG method; RPIM formulation; phase field fracture; meshfree scheme.
AMS Subject Classification 2010: 74R10, 74S30, 65N99, 35Q74.

1 Introduction

Ensuring structural integrity through fracture analysis remains a fundamental objective in modern engineering design. The classical theory of brittle fracture, initiated by Griffith [14] and later refined by Irwin [19] and Rice [29], models cracks as sharp discontinuities embedded within a continuous medium. While Linear Elastic Fracture Mechanics (LEFM) provides a rigorous theoretical framework, its numerical implementation using the Finite Element Method (FEM) encounters well-known limitations. In particular, the simulation of complex crack phenomena such as branching, coalescence, and arbitrary

*Corresponding author
Received: 14 March 2026/ Revised: 13 November 2026/ Accepted: 14 November 2026
DOI: 10.22124/jmm.2026.33175.3021

© 2026 University of Guilan

Corrected Proof

propagation paths typically requires costly remeshing procedures or enrichment strategies, including the Extended Finite Element Method (XFEM) [26]. Compared with the standard finite element method, XFEM offers significant advantages for fracture simulations: enrichment functions allow discontinuities and crack-tip singularities to be represented without remeshing, so crack propagation can be captured independently of the underlying mesh topology.

To overcome these challenges, Phase-Field Fracture (PFF) models have emerged as a powerful alternative; comprehensive reviews have highlighted their rapid development and application to brittle materials, composites, and engineering structures [2]. Based on the variational energy minimization framework of Francfort and Marigo [12], regularized for numerical implementation by Bourdin et al. [9, 10, 33], the phase-field approach replaces sharp crack discontinuities with a diffusive damage zone governed by a scalar order parameter. This formulation enables crack initiation, branching, and merging to occur naturally without explicit tracking. Significant advancements include thermodynamically consistent formulations [24], staggered solution algorithms for improved robustness [25], and energy decomposition techniques to prevent unphysical crack growth under compression [4, 34].

Despite these theoretical advantages, FEM-based phase-field implementations remain sensitive to mesh quality and may suffer from interpolation constraints in highly localized damage zones. Meshfree methods provide an attractive alternative by eliminating fixed element connectivity and offering higher geometric flexibility. Early meshfree schemes such as the Element-Free Galerkin (EFG) method [7] and the Reproducing Kernel Particle Method (RKPM) [21] demonstrated promising capabilities. However, the Moving Least Squares (MLS) approximation typically employed in EFG lacks the Kronecker delta property, complicating the imposition of essential boundary conditions [38].

The Meshless Local Petrov–Galerkin (MLPG) method, introduced by Atluri and Zhu [5,6], addresses several of these issues by employing local weak forms over small subdomains and avoiding the need for a global background mesh. This feature makes MLPG particularly suitable for problems involving evolving discontinuities. In recent years, the method and its localized variants have undergone substantial theoretical and computational advancements. Adaptive multi-resolution MLPG formulations have been proposed to enhance accuracy and computational efficiency in nonlinear systems [31]. Rigorous mathematical analyses and novel extensions, including localized meshless approaches for nonlinear Sobolev equations [16], have further strengthened the stability and convergence properties of these methods [13]. Moreover, enhanced meshless frameworks have been successfully applied to microscale heat transfer processes [28], complex nonlinear flow problems, and multiphysics simulations [11, 17], demonstrating the method's robustness and versatility in handling strongly coupled partial differential equations. Recent developments in meshfree and RPIM-based numerical techniques have also demonstrated their effectiveness for solving coupled multiphysics and nonlinear PDE systems, e.g. hydroelastic problems [18] and reaction–diffusion systems [1].

To facilitate the enforcement of essential boundary conditions within a meshfree context, the Radial Point Interpolation Method (RPIM) [22, 32] offers shape functions satisfying the Kronecker delta property, thereby simplifying numerical implementation. Recent research has increasingly explored the integration of meshfree discretizations with variational phase-field formulations, including multiscale strategies [35], natural neighbor Galerkin approaches [20], adaptive EFG-based fracture modeling [30], and higher-order phase-field theories [3]. These studies collectively indicate a growing interest in combining the geometric flexibility of meshfree methods with the variational rigor of phase-field fracture modeling.

Motivated by these developments, the present study develops an MLPG-RPIM computational frame-

Corrected Proof

work for solving the coupled nonlinear equations governing phase-field fracture. A spectral decomposition of the strain tensor [25] is used to distinguish tensile and compressive contributions in the constitutive response. The framework combines local MLPG integration with RPIM-based field approximation and is assessed using a series of two-dimensional benchmark problems, including those involving strongly heterogeneous materials [27]. We emphasize from the outset that the proposed formulation is meshfree in its approximation and nodal connectivity; Cartesian background cells are used only as integration subdomains and do not constitute a field-approximation mesh.

The contribution of the present work is the formulation and numerical assessment of an MLPG-RPIM approach for phase-field fracture. Specifically, the work includes:

- **Discretization:** Formulation of an MLPG-RPIM discretization for the coupled displacement and phase-field equations.
- **Numerical integration:** Use of local integration domains and test functions within the MLPG formulation to evaluate the governing equations without relying on a predefined global element connectivity.
- **Constitutive implementation:** Incorporation of a spectral strain decomposition into the meshfree formulation to distinguish tensile and compressive contributions to the constitutive response.
- **Benchmark assessment:** Evaluation of the formulation using two-dimensional benchmark problems, with the relevant model parameters and implementation details reported in Table 1.

2 Variational formulation of phase-field fracture

2.1 Energy functional and crack-surface regularization

Let $\Omega \subset \mathbb{R}^d$ ($d \in \{2,3\}$) be an open, bounded domain with a Lipschitz continuous boundary $\partial\Omega = \Gamma_u \cup \Gamma_t$ such that $\Gamma_u \cap \Gamma_t = \emptyset$ and $\text{meas}(\Gamma_u) > 0$. The body is subjected to prescribed Dirichlet data $\bar{\mathbf{u}}$ on Γ_u, surface tractions $\bar{\mathbf{t}}$ on Γ_t, and volumetric body forces $\mathbf{b} \in [L^2(\Omega)]^d$.

In the classical Griffith theory, a crack propagates when the energy release rate exceeds the critical fracture toughness G_c. Numerically tracking an evolving sharp interface $\mathscr{C}$ requires complex remeshing or enrichment. Following Francfort and Marigo [12] and Bourdin et al. [9, 10], the sharp crack is regularized into a continuous, diffusive topology via a scalar phase-field variable $d(\mathbf{x},t) \in [0,1]$, where $d = 0$ denotes intact material and $d = 1$ fully broken material, over a length scale $\ell_0 > 0$. The total potential energy functional $\Pi : \mathscr{U} \times \mathscr{W} \to \mathbb{R}$ of the fracturing continuum is

$$\Pi(\mathbf{u},d) = \int_\Omega \psi(\boldsymbol{\varepsilon}(\mathbf{u}),d)\,\mathrm{d}\Omega + G_c \int_\Omega \gamma(d,\nabla d)\,\mathrm{d}\Omega - \int_\Omega \mathbf{b}\cdot\mathbf{u}\,\mathrm{d}\Omega - \int_{\Gamma_t} \bar{\mathbf{t}}\cdot\mathbf{u}\,\mathrm{d}\Gamma, \tag{1}$$

where $G_c > 0$ is the critical energy release rate, $\boldsymbol{\varepsilon}(\mathbf{u}) = \frac{1}{2}(\nabla\mathbf{u} + \nabla\mathbf{u}^T)$ is the infinitesimal strain tensor, and the AT_2 crack surface density is

$$\gamma(d,\nabla d) = \frac{1}{2\ell_0}d^2 + \frac{\ell_0}{2}|\nabla d|^2. \tag{2}$$

To prevent unphysical crack growth under compression, the elastic strain energy density $\psi(\boldsymbol{\varepsilon},d)$ is additively split into damaged tensile and intact compressive parts via the spectral decomposition of $\boldsymbol{\varepsilon}$:

$$\psi(\boldsymbol{\varepsilon},d) = g(d)\,\psi_0^+(\boldsymbol{\varepsilon}) + \psi_0^-(\boldsymbol{\varepsilon}), \tag{3}$$

Corrected Proof

with

$$\psi_0^{\pm}(\varepsilon) = \frac{1}{2}\lambda \langle \mathrm{tr}(\varepsilon)\rangle_{\pm}^2 + \mu\, \mathrm{tr}(\varepsilon_{\pm}^2), \tag{4}$$

where λ, μ are the Lamé constants, $\langle x\rangle_{\pm} = (x \pm |x|)/2$ are the Macaulay brackets, and $\varepsilon_{\pm}$ are defined in Section 2.2. The degradation function is taken throughout this work as

$$g(d) = (1-d)^2 + \kappa, \qquad g(0) = 1+\kappa, \quad g(1) = \kappa, \tag{5}$$

with a residual-stiffness parameter $0 < \kappa \ll 1$ (here $\kappa = 10^{-6}$). We stress that g is *not* normalized: $g(0) = 1+\kappa$ is used as written, so κ appears exactly once, inside $g(d)$, and never as an additional additive term elsewhere.

Substituting (2)–(5) into (1) yields the regularized energy

$$\Pi_{\ell_0}(\mathbf{u}, d) = \int_\Omega \left[g(d)\psi_0^+(\varepsilon) + \psi_0^-(\varepsilon)\right] \mathrm{d}\Omega + G_c \int_\Omega \left[\frac{1}{2\ell_0} d^2 + \frac{\ell_0}{2}|\nabla d|^2\right] \mathrm{d}\Omega - \int_\Omega \mathbf{b}\cdot\mathbf{u}\,\mathrm{d}\Omega - \int_{\Gamma_t} \bar{\mathbf{t}}\cdot\mathbf{u}\,\mathrm{d}\Gamma. \tag{6}$$

2.2 Constitutive relations and spectral decomposition

For $\mathbf{u} = [u_1, u_2]^T$ in two dimensions, the symmetric strain tensor is

$$\varepsilon(\mathbf{u}) = \begin{bmatrix} \varepsilon_{11} & \varepsilon_{12} \\ \varepsilon_{12} & \varepsilon_{22} \end{bmatrix} = \begin{bmatrix} \partial_x u_1 & \frac{1}{2}(\partial_y u_1 + \partial_x u_2) \\ \frac{1}{2}(\partial_y u_1 + \partial_x u_2) & \partial_y u_2 \end{bmatrix}, \tag{7}$$

with out-of-plane components vanishing under plane strain ($\varepsilon_{33} = \varepsilon_{13} = \varepsilon_{23} = 0$).

Following Miehe et al. [24] and Wick [33], the spectral decomposition of ε reads

$$\varepsilon = \sum_{a=1}^{d} \varepsilon_a\, \mathbf{n}_a \otimes \mathbf{n}_a, \tag{8}$$

where ε_a and $\mathbf{n}_a$ are the principal strains and orthonormal principal directions. In 2D, the principal strains are

$$\varepsilon_{1,2} = \frac{\varepsilon_{11}+\varepsilon_{22}}{2} \pm \sqrt{\left(\frac{\varepsilon_{11}-\varepsilon_{22}}{2}\right)^2 + \varepsilon_{12}^2}. \tag{9}$$

The positive and negative parts are

$$\varepsilon_+ = \sum_{a=1}^{d} \langle \varepsilon_a\rangle_+\, \mathbf{n}_a \otimes \mathbf{n}_a, \qquad \varepsilon_- = \sum_{a=1}^{d} \langle \varepsilon_a\rangle_-\, \mathbf{n}_a \otimes \mathbf{n}_a, \tag{10}$$

satisfying $\varepsilon = \varepsilon_+ + \varepsilon_-$.

The Cauchy stress follows from $\boldsymbol{\sigma} = \partial\psi/\partial\varepsilon$, consistently with (3)–(5):

$$\boldsymbol{\sigma} = g(d)\,\boldsymbol{\sigma}^+ + \boldsymbol{\sigma}^-, \qquad \boldsymbol{\sigma}^{\pm} = \lambda \langle \mathrm{tr}(\varepsilon)\rangle_{\pm} \boldsymbol{I} + 2\mu\, \varepsilon_{\pm}, \tag{11}$$

so that κ enters only through $g(d)$ and is never added separately to $\boldsymbol{\sigma}^+$. Compressive stress paths ($\boldsymbol{\sigma}^-$) retain their full elastic capacity, precluding interpenetration of the diffusive crack faces.

Corrected Proof

2.3 Strong form and irreversibility

The first Gâteaux variation of Π_{ℓ_0} with respect to $\mathbf{u}$ in any admissible direction $\mathbf{v} \in \mathscr{V}_0 = \{\mathbf{v} \in [H^1(\Omega)]^d \mid \mathbf{v} = \mathbf{0} \text{ on } \Gamma_u\}$ gives, after integration by parts,

$$\nabla \cdot \boldsymbol{\sigma} + \mathbf{b} = \mathbf{0} \text{ in } \Omega, \qquad \boldsymbol{\sigma}\mathbf{n} = \bar{\mathbf{t}} \text{ on } \Gamma_t, \qquad \mathbf{u} = \bar{\mathbf{u}} \text{ on } \Gamma_u. \tag{12}$$

Similarly, the variation with respect to d in any $w \in H^1(\Omega)$ yields

$$\frac{\partial \psi}{\partial d} + \frac{G_c}{\ell_0} d - G_c \ell_0 \nabla^2 d = 0 \text{ in } \Omega, \qquad \nabla d \cdot \mathbf{n} = 0 \text{ on } \partial\Omega. \tag{13}$$

To enforce irreversibility ($\dot{d} \geq 0$) and monotone crack growth, the history field

$$\mathscr{H}(\mathbf{x}, t) = \max_{\tau \in [0,t]} \psi_0^+(\boldsymbol{\varepsilon}(\mathbf{u}(\mathbf{x}, \tau))) \tag{14}$$

replaces ψ_0^+ in the driving force $\partial\psi/\partial d = -2(1-d)\mathscr{H}$. The derivative of $g(d) = (1-d)^2 + \kappa$ with respect to d is $-2(1-d)$; the constant κ contributes nothing to the driving force, consistent with its role as a residual stiffness. The complete coupled strong-form problem is

$$\begin{cases} \nabla \cdot \boldsymbol{\sigma} + \mathbf{b} = \mathbf{0} & \text{in } \Omega, \\ \left(\frac{G_c}{\ell_0} + 2\mathscr{H}\right) d - G_c \ell_0 \nabla^2 d = 2\mathscr{H} & \text{in } \Omega, \\ \mathbf{u} = \bar{\mathbf{u}} & \text{on } \Gamma_u, \\ \boldsymbol{\sigma}\mathbf{n} = \bar{\mathbf{t}} & \text{on } \Gamma_t, \\ \nabla d \cdot \mathbf{n} = 0 & \text{on } \partial\Omega. \end{cases} \tag{15}$$

2.4 Abstract weak formulation

Define the spaces

$$\mathscr{U} = \{\mathbf{u} \in [H^1(\Omega)]^d \mid \mathbf{u} = \bar{\mathbf{u}} \text{ on } \Gamma_u\}, \tag{16}$$

$$\mathscr{V}_0 = \{\mathbf{v} \in [H^1(\Omega)]^d \mid \mathbf{v} = \mathbf{0} \text{ on } \Gamma_u\}, \tag{17}$$

$$\mathscr{W} = H^1(\Omega). \tag{18}$$

Mechanical subproblem. Given $d \in \mathscr{W}$, find $\mathbf{u} \in \mathscr{U}$ such that

$$a_u(\mathbf{u}, \mathbf{v}; d) = l_u(\mathbf{v}) \quad \forall \mathbf{v} \in \mathscr{V}_0, \tag{19}$$

with

$$a_u(\mathbf{u}, \mathbf{v}; d) = \int_\Omega \boldsymbol{\sigma}(\mathbf{u}, d) : \boldsymbol{\varepsilon}(\mathbf{v}) \, \mathrm{d}\Omega, \tag{20}$$

$$l_u(\mathbf{v}) = \int_\Omega \mathbf{b} \cdot \mathbf{v} \, \mathrm{d}\Omega + \int_{\Gamma_t} \bar{\mathbf{t}} \cdot \mathbf{v} \, \mathrm{d}\Gamma. \tag{21}$$

Corrected Proof

Phase-field subproblem. Given $\mathscr{H} \in L^2(\Omega)$, find $d \in \mathscr{W}$ such that

$$a_d(d, w; \mathscr{H}) = l_d(w; \mathscr{H}) \quad \forall w \in \mathscr{W}, \tag{22}$$

with the symmetric bilinear form and linear functional

$$a_d(d, w; \mathscr{H}) = \int_\Omega \left[\left(\frac{G_c}{\ell_0} + 2\mathscr{H} \right) d\, w + G_c \ell_0 \nabla d \cdot \nabla w \right] \mathrm{d}\Omega, \tag{23}$$

$$l_d(w; \mathscr{H}) = \int_\Omega 2\mathscr{H}\, w \, \mathrm{d}\Omega. \tag{24}$$

Well-posedness. Since $G_c > 0$, $\ell_0 > 0$ and $\mathscr{H} \geq 0$ a.e., a_d is symmetric, bounded and $H^1(\Omega)$-elliptic:

$$a_d(w, w; \mathscr{H}) \geq \frac{G_c}{\ell_0} \|w\|^2_{L^2(\Omega)} + G_c \ell_0 \|\nabla w\|^2_{L^2(\Omega)} \geq C_0 \|w\|^2_{H^1(\Omega)}, \tag{25}$$

with $C_0 = \min\{G_c/\ell_0, G_c\ell_0\} > 0$. By the Lax–Milgram lemma, (22) has a unique solution $d \in H^1(\Omega)$ for any admissible displacement state.

The coupled continuous problem is

$$\begin{cases} a_u(\mathbf{u}, \mathbf{v}; d) = l_u(\mathbf{v}) & \forall \mathbf{v} \in \mathscr{V}_0, \\ a_d(d, w; \mathscr{H}) = l_d(w; \mathscr{H}) & \forall w \in \mathscr{W}. \end{cases} \tag{26}$$

Equations (19) and (22) are the continuous equations projected onto local Petrov–Galerkin subdomains in Section 4.

3 Radial point interpolation method (RPIM)

Notation used throughout Sections 3–6 is summarized here. Let L be the side of the square computational domain, N_x the number of nodes per side, and $h_s := L/(N_x - 1)$ the nominal nodal spacing. The average spacing used inside the RPIM support is $d_c := h_s$. The support radius is $r_s = \alpha_s d_c$, distinct from both h_s and the phase-field length scale ℓ_0. The history field is $\mathscr{H}$, the damage variable is d, and the displacement vector is $\mathbf{u}$.

A fundamental aspect of the current MLPG approach is the generation of shape functions using RPIM, which allows field interpolation over scattered nodes without a global grid [22, 32]. Further theoretical aspects can be found in [15].

3.1 Construction of shape functions

For a point of interest $\mathbf{x} \in \Omega$, consider a local support domain containing n field nodes at $\mathbf{x}_1, \ldots, \mathbf{x}_n$. The RPIM approximation is

$$u^h(\mathbf{x}) = \sum_{i=1}^{n} R_i(\mathbf{x}) a_i + \sum_{j=1}^{m} p_j(\mathbf{x}) b_j = \mathbf{R}^T(\mathbf{x})\mathbf{a} + \mathbf{P}^T(\mathbf{x})\mathbf{b}, \tag{27}$$

Corrected Proof

where m is the number of polynomial terms (linear consistency in 2D: $m=3$, $\mathbf{P}^T(\mathbf{x})=[1,x,y]$). Enforcing interpolation at the n support nodes and the orthogonality constraint $\sum_i p_j(\mathbf{x}_i)a_i=0$ yields

$$\begin{bmatrix}\mathbf{G} & \mathbf{P}_m\\ \mathbf{P}_m^T & \mathbf{0}\end{bmatrix}\begin{Bmatrix}\mathbf{a}\\ \mathbf{b}\end{Bmatrix}=\begin{Bmatrix}\mathbf{u}_s\\ \mathbf{0}\end{Bmatrix}, \tag{28}$$

with $[\mathbf{G}]_{ij}=R(\|\mathbf{x}_j-\mathbf{x}_i\|)$ and $[\mathbf{P}_m]_{ij}=p_j(\mathbf{x}_i)$. In this work we use the Multiquadrics (MQ) kernel

$$R_i(\mathbf{x})=(r_i^2+c^2)^q, \qquad r_i=\|\mathbf{x}-\mathbf{x}_i\|, \tag{29}$$

with shape parameters $q=1.03$ and $c=1.42\,d_c$, where d_c is the average nodal spacing defined above.

Inverting (28) and substituting back gives

$$u^h(\mathbf{x})=\sum_{I=1}^{n}\Phi_I(\mathbf{x})u_I, \qquad \mathbf{\Phi}^T(\mathbf{x})=[\mathbf{R}^T(\mathbf{x}),\mathbf{P}^T(\mathbf{x})]\,\mathbf{A}^{-1}\begin{bmatrix}\mathbf{I}_n\\ \mathbf{0}\end{bmatrix}, \tag{30}$$

where $\mathbf{A}$ is the system matrix in (28).

3.2 Spatial derivatives

Because $\mathbf{A}$ depends only on nodal coordinates,

$$\frac{\partial\mathbf{\Phi}^T(\mathbf{x})}{\partial\xi}=\left[\frac{\partial\mathbf{R}^T}{\partial\xi},\frac{\partial\mathbf{P}^T}{\partial\xi}\right]\mathbf{A}^{-1}\begin{bmatrix}\mathbf{I}_n\\ \mathbf{0}\end{bmatrix}, \quad \xi\in\{x,y\}, \qquad \frac{\partial R_i}{\partial\xi}=2q(r_i^2+c^2)^{q-1}(\xi-\xi_i). \tag{31}$$

3.3 Influence (support) domain

The support domain Ω_s of a quadrature point $\mathbf{x}_Q$ is a disk of radius

$$r_s=\alpha_s\,d_c, \qquad \alpha_s=3.2, \tag{32}$$

where d_c is the average nodal spacing. The support is truncated by the domain boundary; if fewer than 6 nodes remain inside Ω_s, the radius is enlarged locally by 20% until the minimum is met. The number of active nodes reported in Table 1 ($N_s\approx 16$–25) is an approximate range and varies with location and refinement. This is illustrated in Figure 1.

4 MLPG discretization and staggered scheme

As noted above, the approximation and nodal connectivity are meshfree; the Cartesian background cells introduced in this section are used only as integration subdomains and do not constitute a field-approximation mesh or a global element connectivity.

4.1 Local weak form

For each node Q, let Ω_Q be its local subdomain. Restricting (23) to Ω_Q with test function ψ gives

$$\int_{\Omega_Q}\left[\left(\frac{G_c}{\ell_0}+2\mathscr{H}\right)d\,\psi+G_c\ell_0\nabla d\cdot\nabla\psi\right]\mathrm{d}\Omega=\int_{\Omega_Q}2\mathscr{H}\,\psi\,\mathrm{d}\Omega. \tag{33}$$

Corrected Proof

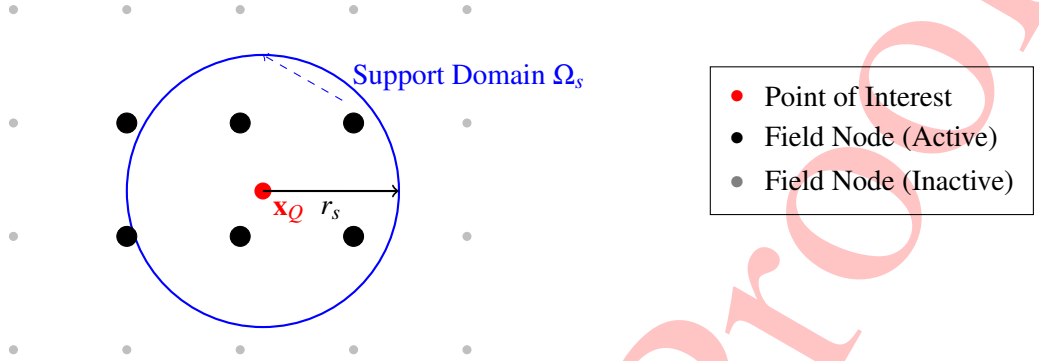


Figure 1: Local support domain Ω_s for a quadrature point $\mathbf{x}_Q$; only nodes within r_s contribute to the shape functions.

4.2 Discretized systems

Phase-field. Substituting $d^h(\mathbf{x}) = \sum_J \Phi_J(\mathbf{x}) d_J$ into (33) gives $\mathbf{K}^d \mathbf{d} = \mathbf{F}^d$ with

$$\mathbf{K}^d_{IJ} = \int_{\Omega_Q} \left[\left(\frac{G_c}{\ell_0} + 2\mathscr{H} \right) \Phi_I \Phi_J + G_c \ell_0 (\nabla \Phi_I \cdot \nabla \Phi_J) \right] \mathrm{d}\Omega, \tag{34}$$

$$\mathbf{F}^d_I = \int_{\Omega_Q} 2\mathscr{H}\, \Phi_I \, \mathrm{d}\Omega. \tag{35}$$

Mechanical system. The assembled stiffness uses the secant operator $\mathbf{C}(d) = g(d)\mathbb{C}^+ + \mathbb{C}^-$ with $g(d) = (1-d)^2 + \kappa$ from (5); note that κ enters only through $g(d)$ and the stress is (11). The consistent algorithmic tangent $\mathbb{C}_{\text{alg}} = \partial \boldsymbol{\sigma} / \partial \boldsymbol{\varepsilon}$ is not used in the staggered solve; the secant operator provides unconditional stability at the cost of a linear, rather than quadratic, convergence rate within each staggered step.

4.3 Staggered algorithm

The denominators use $\max(\|\cdot\|_2, \varepsilon)$ with $\varepsilon = 10^{-14}$ to guard against a vanishing reference norm. The same criteria and the same 50-iteration cap are used in every benchmark. If the cap is reached without satisfying the tolerance, the increment is flagged and reported in the solver log; none of the runs reported below reached the cap.

4.4 Implementation and numerical details

1. **RPIM parameters.** MQ kernel with $q = 1.03$, $c = 1.42\, d_c$, linear polynomial basis ($m = 3$), support radius $r_s = 3.2\, d_c$, minimum 6 support nodes. See Section 3.1 for the definitions of d_c, r_s, c and the boundary handling.
2. **Numerical quadrature.** A Cartesian background mesh is used solely for integration. A 4×4 Gauss–Legendre rule is applied to bulk cells; a 6×6 rule is applied to cells whose centroid $\mathbf{x}$ satisfies $\mathrm{dist}(\mathbf{x}, \Gamma_c) \le 2\ell_0$ or $\mathscr{H}(\mathbf{x}) > 0$, which identifies the fracture-process zone (FPZ). The same rule is used in every benchmark and every refinement.

Corrected Proof

Algorithm 1 Staggered MLPG-RPIM scheme for phase-field fracture

Input: $\mathbf{U}_0$, $\mathbf{D}_0$, $\mathscr{H}_0 = 0$, $tol = 10^{-5}$, $k_{\max} = 50$.
Output: $\mathbf{U}_N$, $\mathbf{D}_N$, $\mathscr{H}_N$.
for $n = 1, 2, \ldots, N_{\text{steps}}$ **do**
  $\mathbf{D}^{(0)} = \mathbf{D}_{n-1}$
  for $k = 0, 1, \ldots, k_{\max}$ **do**
    Mechanical step: solve $\mathbf{K}^u(\mathbf{D}^{(k)})\,\mathbf{U}^{(k+1)} = \mathbf{F}_n^{\text{ext}}$
    History update: $\mathscr{H}^{(k+1)} = \max\left(\mathscr{H}_n,\ \psi^+(\boldsymbol{\varepsilon}(\mathbf{U}^{(k+1)}))\right)$
    Phase-field step: solve $\mathbf{K}^d(\mathscr{H}^{(k+1)})\,\mathbf{D}^{(k+1)} = \mathbf{F}^d(\mathscr{H}^{(k+1)})$
    if $\dfrac{\|\mathbf{D}^{(k+1)} - \mathbf{D}^{(k)}\|_2}{\max(\|\mathbf{D}^{(k+1)}\|_2, \varepsilon)} < tol$ **and** $\dfrac{\|\mathbf{U}^{(k+1)} - \mathbf{U}^{(k)}\|_2}{\max(\|\mathbf{U}^{(k+1)}\|_2, \varepsilon)} < tol$ **then**
      break
    end if
  end for
  $\mathbf{U}_n = \mathbf{U}^{(k+1)}$, $\mathbf{D}_n = \mathbf{D}^{(k+1)}$, $\mathscr{H}_n = \mathscr{H}^{(k+1)}$
end for

3. **History storage.** $\mathscr{H}$ is stored at Gauss points and updated as $\mathscr{H}_{n+1}(\mathbf{x}_g) = \max\{\mathscr{H}_n(\mathbf{x}_g), \psi_0^+(\boldsymbol{\varepsilon}_{n+1}(\mathbf{x}_g))\}$.
4. **Pre-crack.** The pre-crack is imposed by a dual scheme, exactly as summarized in Table 1: (i) $d = 1$ is prescribed on the nodes lying on the crack line Γ_c; and (ii) $\mathscr{H}_0(\mathbf{x}_g)$ is initialized at Gauss points by

$$\mathscr{H}_0(\mathbf{x}_g) = \begin{cases} \dfrac{G_c}{2\ell_0}\left(1 - \dfrac{2\,\text{dist}(\mathbf{x}_g, \Gamma_c)}{\ell_0}\right), & \text{dist}(\mathbf{x}_g, \Gamma_c) \le \ell_0/2, \\ 0, & \text{otherwise.} \end{cases} \tag{36}$$

   The bulk is initialized with $d = 0$; the only place where $d = 1$ is used at $t = 0$ is the crack-line node set in (i).
5. **Convergence and solver.** Relative criteria and the 50-iteration cap as in Section 4.3; linear systems solved with MATLAB's sparse direct factorization (SuiteSparse/CHOLMOD). Dirichlet data are enforced with the direct penalty method ($\alpha_{\text{pen}} = 10^{14}$). The damage field is clipped to $[0, 1]$ after each solve.

5 Numerical benchmarks

All simulations are two-dimensional and, unless explicitly stated otherwise, use plane strain ($\varepsilon_{zz} = 0$); this assumption is repeated at the point where each benchmark is introduced. Reaction forces are reported in kN, displacements in mm, G_c in N/mm ($= 10^{-3}$ kN/mm), E in MPa, and ℓ_0, h_s, d_c in mm. A uniform nodal distribution is used. A constant step $\Delta t = 0.01$ (pseudo-time, monotone loading) with $\Delta u = 10^{-5}$ mm per step is used, giving 200 equal load steps; t carries no physical time scale and is used only to enforce $d_{n+1} \ge d_n$. The baseline grid is 27×27 ($N = 729$), and the convergence study uses the finer 51×51 ($N = 2{,}601$) and 101×101 ($N = 10{,}201$) grids. Throughout, $h_s := L/(N_x - 1)$ is the nominal nodal spacing and $d_c := h_s$ the average spacing used in the RPIM support; these conventions are used consistently in the parameter table, the convergence tables, and the RPIM support formulas.

Corrected Proof

On the resolution of the length scale. The phase-field length scale is $\ell_0 = 0.015$ mm. For the baseline 27×27 grid, $h_s/\ell_0 \approx 2.57$; for the finer grids, $h_s/\ell_0 \approx 1.33$ (51×51) and ≈ 0.67 (101×101). While a strict resolution requirement of $h_s \leq \ell_0/2$ is often cited in the literature as a conservative rule of thumb, it is not a strict mathematical necessity for the variational formulation to converge. As demonstrated in previous studies (e.g., [24, 30]), reliable and convergent phase-field results can be obtained when the damage band is resolved by at least one or two elements, i.e., $h_s \lesssim \ell_0$. In this work, the quantitative results are reported exclusively on the 51×51 and 101×101 grids, which fall within this practical range ($h_s/\ell_0 \lesssim 1.33$). The convergence trend from 51×51 to 101×101 confirms that the results are approaching the reference FEM/XFEM solutions. The baseline 27×27 grid ($h_s/\ell_0 \approx 2.57$) is used solely for qualitative visualizations (crack paths) and no quantitative claims are made based on it.

Three separate assessments. We distinguish explicitly: (i) convergence with respect to h_s, assessed by comparing the 51×51 and 101×101 rows of each table; (ii) sensitivity to the ratio h_s/ℓ_0, reported as a dedicated column in each table, without claiming that the recommended $h_s \leq \ell_0/2$ is met; (iii) agreement with external reference solutions, reported only for the peak reaction force and the displacement at peak load. No trend across the tested grids is interpreted as proof of mesh independence.

Scope of validation. Validation in this work is limited to (i) the peak reaction force, (ii) the displacement at peak load, and (iii) a qualitative comparison of crack paths. A curve-based error measure (e.g. an L^2 norm of the load–displacement difference on a common grid) and a quantitative crack-path metric (e.g. a Hausdorff distance between predicted and reference paths) were not computed in this study. Accordingly, statements about agreement are restricted to the quantities actually reported, and no claim of comprehensive quantitative agreement is made.

To ensure transparency and deterministic reproducibility, the complete set of parameters is summarized in Table 1. The damage field is initialized as described in Section 4.4: $d = 0$ in the bulk, and $d = 1$ on the crack-line nodes together with the history initialization (36).

5.1 Validation and comparative analysis

The single edge notched tension test is first performed as a validation case. The crack path and the peak load are compared with FEM and XFEM results reported by [24] and [23]. The peak load and displacement at peak load agree with the FEM/XFEM references to within the errors reported in Table 2; the post-peak response and the crack trajectory are compared qualitatively (Figures 3 and 2), since no curve-based error or crack-path metric was computed.

Remark 1. ***Computational performance.*** The CPU times in the tables are implementation-specific reference values, not absolute performance metrics. Simulations were run on a desktop with an Intel Core i5-12500H (up to 4.5 GHz) and 16 GB of RAM, in MATLAB R2014b (64-bit). Linear systems are solved with the built-in sparse direct solver. For the paired comparison at comparable resolution, the 101×101 MLPG-RPIM run (10,201 nodes, 20,402 DOF) and the 30,000-element FEM reference (60,000 DOF) differ in DOF counts and solver tolerances; their wall-clock times are reported in Table 2 for that specific pair, and no uniform ratio across all cases is claimed.

5.2 Single edge notched specimen: Tension test

The specimen is a 1 mm square with a 0.5 mm horizontal pre-notch. The bottom edge is fixed and a vertical displacement is applied to the top edge; the crack is expected to grow horizontally. The setup

Corrected Proof

Table 1: Complete reproducible parameter specifications for the numerical benchmarks (MLPG–RPIM implementation)

Category	Parameter / Implementation Detail	Value / Specification
Geometry & Mesh	Specimen dimensions ($L \times H$)	1.0×1.0 mm (SENT & Shear)
	Initial crack position & length	Mid-height ($y = 0.5$ mm), length $a = 0.5$ mm
	Node distribution ($N_x \times N_y$)	27×27 regular nodal grid ($N = 729$ nodes)
	Nominal spacing ($h_s = L/(N_x - 1)$)	0.0385 mm
	Average spacing for RPIM (d_c)	$d_c = h_s$
Constitutive & Fracture	Young's modulus (E)	210×10^3 MPa
	Poisson's ratio (ν)	0.3
	Fracture energy (G_c)	2.7 N/mm ($= 2.7 \times 10^{-3}$ kN/mm)
	Regularization length scale (ℓ_0)	0.015 mm
	Residual stiffness parameter (κ)	10^{-6}
	Formulation state	Plane strain ($\mathbf{C}(d) = g(d)\mathbb{C}^+ + \mathbb{C}^-$)
RPIM Shape Functions	Radial Basis Function (RBF)	Multiquadrics: $R_i = (r_i^2 + c^2)^q$
	Shape parameters	$q = 1.03$, $c = 1.42\, d_c$
	Polynomial basis	Linear complete ($m = 3$: $[1, x, y]$)
	Influence/support radius (r_s)	$3.2\, d_c$
	Minimum support nodes	6 nodes (support enlarged by 20% if fewer)
Domain Integration	Background cell arrangement	Cartesian quadrilateral cells (integration only)
	Quadrature rule for bulk cells	4×4 Gauss–Legendre ($n_{\text{GP}} = 16$)
	Quadrature rule for FPZ cells	6×6 Gauss–Legendre ($n_{\text{GP}} = 36$)
	FPZ identification rule	$\text{dist}(\mathbf{x}, \Gamma_c) \leq 2\ell_0$ or $\mathscr{H}(\mathbf{x}) > 0$
	Local subdomain Ω_s	Congruent with background integration cells
Algorithmic & Solver	Boundary condition enforcement	Direct penalty method ($\alpha_{\text{pen}} = 10^{14}$)
	Staggered convergence metric	$\| .^{(k+1)} - .^{(k)} \|_2 / \max(\| .^{(k+1)} \|_2, \varepsilon) < 10^{-5}$, $\varepsilon = 10^{-14}$
	Maximum staggered iterations	50 per increment (none of the runs reached the cap)
	Monotonicity & admissibility	Monotonic $\mathscr{H}_{n+1}$, $d \in [0, 1]$ projection
	Pre-crack initialization	Dual scheme: $d = 1$ on crack-line nodes and $\mathscr{H}_0(\mathbf{x}_g)$ via Eq. (36)
	Displacement increment	$\Delta u = 1.0 \times 10^{-5}$ mm (200 equal load steps)
	Linear solver	Direct sparse factorization (SuiteSparse / CHOLMOD)

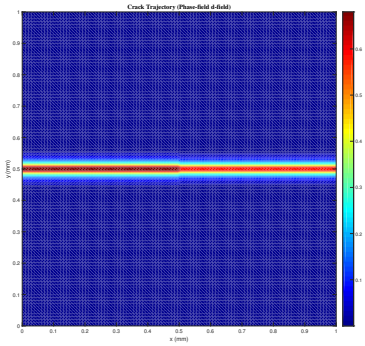


Figure 2: Crack trajectory for the SENT test using the MLPG-RPIM phase-field model, plotted on the 27×27 grid (illustrative only; see the scope discussion in Section 5). The contour is the damage variable d; $d = 1$ indicates a fully developed crack.

Accepted Proof

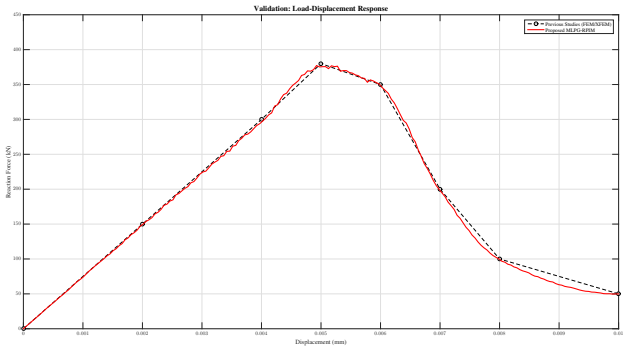


Figure 3: Load–displacement response for the SENT specimen. The solid line is the MLPG-RPIM result; the dashed line is the reference FEM/XFEM result. Peak-load agreement is quantified in Table 2.

is shown in Figure 4. The simulation is plane strain ($\varepsilon_{zz} = 0$). The phase-field evolution is shown in Figures 5–8, all on the 27×27 grid (illustrative). At $t = 0$ the pre-crack is represented by the dual initialization of Section 4.4, namely $d = 1$ on the crack-line nodes together with the history initialization (36). As loading progresses the crack propagates horizontally and the specimen fails.

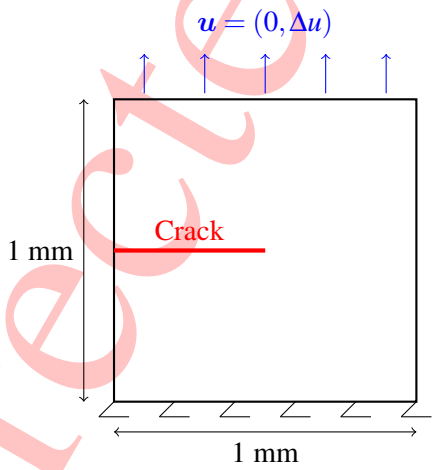


Figure 4: Setup for the single edge notched tension test

Table 2 summarizes the peak reaction force $P_{\max}$, the displacement at peak load u_{crit}, relative errors, h_s/ℓ_0, and CPU times. The 27×27 row is included for reference only; it is not used for any quantitative claim.

5.3 Single edge notched specimen: Pure shear test

A horizontal displacement is prescribed on the upper boundary, inducing mixed-mode behavior. The configuration is shown in Figure 9. Plane strain ($\varepsilon_{zz} = 0$). The crack initiates horizontally and then kinks at approximately 45° (Figures 10–13, all on the 27×27 grid, illustrative).

Corrected Proof

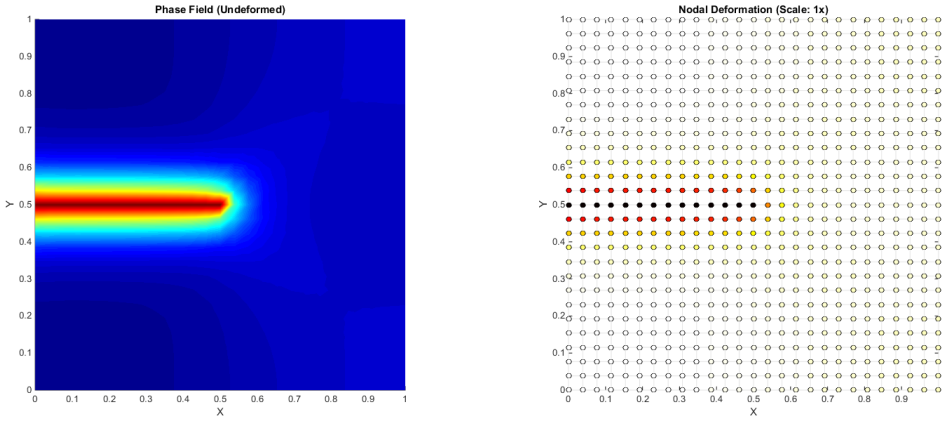


Figure 5: SENT at $t = 0$ (illustrative, 27×27 grid): the pre-crack is represented by the dual initialization of Section 4.4, namely $d = 1$ on the crack-line nodes together with the history initialization (36).

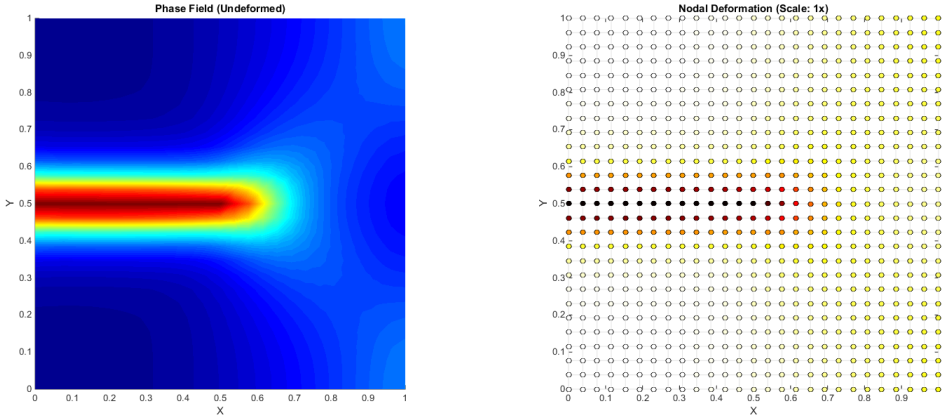


Figure 6: SENT at $t = 50$: (left) phase-field; (right) deformation (illustrative, 27×27)

Table 2: Quantitative comparison for the SENT benchmark ($\ell_0 = 0.015$ mm). The 27×27 row is illustrative-reference only; quantitative claims use the 51×51 and 101×101 rows.

Method / Discretization	**Nodes / Elements**	h_s **[mm]**	h_s/ℓ_0	$P_{\max}$ **[kN]**	**Rel. Error (%)**	u_{crit} **[mm]**	**CPU [s]**
FEM (Miehe et al. [24])	30,000 Elem.	0.0035	0.23	605.2	Ref.	5.85×10^{-3}	280.4
XFEM (Mandal et al. [23])	25,600 Elem.	0.0040	0.27	612.0	+1.12	5.90×10^{-3}	315.0
MLPG-RPIM (illustrative)	27×27 (729)	0.0385	2.57	648.5	+7.15	6.20×10^{-3}	48.2
MLPG-RPIM (Medium)	51×51 (2,601)	0.0200	1.33	618.3	+2.16	5.95×10^{-3}	342.6
MLPG-RPIM (Fine)	101×101 (10,201)	0.0100	0.67	607.8	+0.43	5.87×10^{-3}	3,112.5

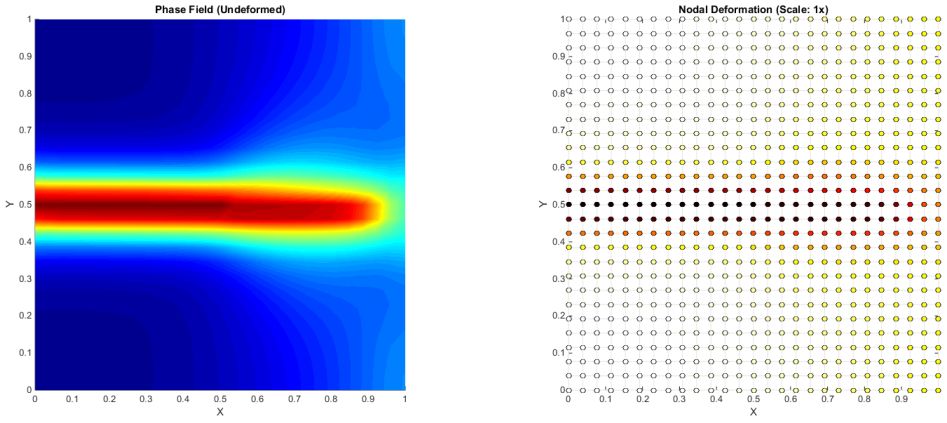


Figure 7: SENT at $t = 100$: (left) phase-field; (right) deformation (illustrative, 27×27)

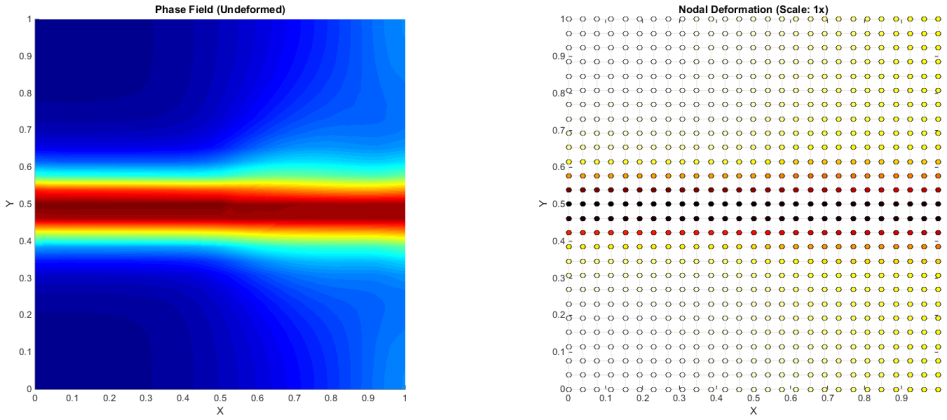


Figure 8: SENT at $t = 200$: (left) phase-field; (right) deformation (illustrative, 27×27)

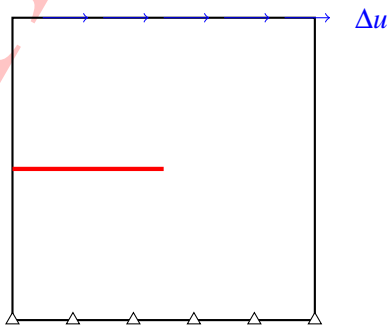


Figure 9: Numerical configuration for the pure shear test

Corrected Proof

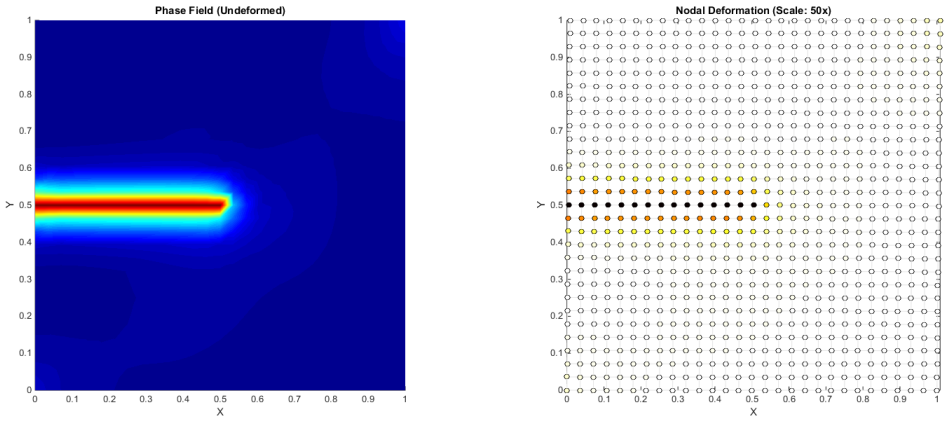


Figure 10: Pure shear at $t = 0$ (illustrative, 27×27 grid): the pre-crack is represented by the dual initialization of Section 4.4, namely $d = 1$ on the crack-line nodes together with the history initialization (36)

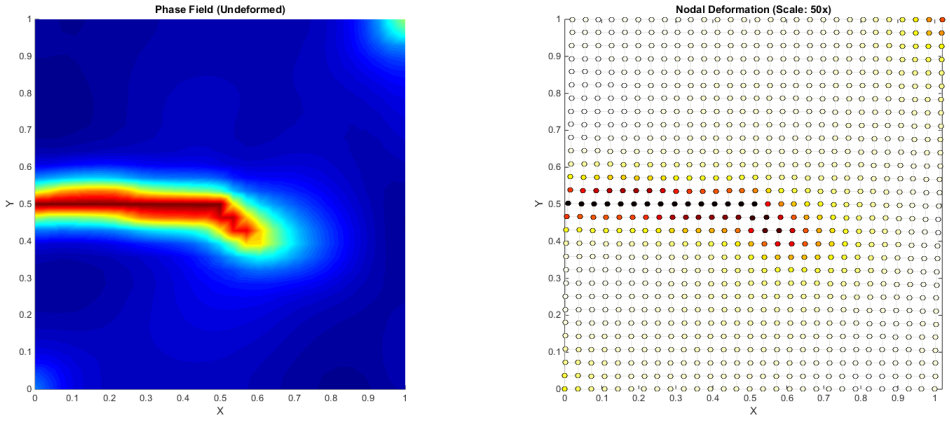


Figure 11: Pure shear at $t = 50$: (left) phase-field; (right) deformation (illustrative, 27×27)

Table 3: Quantitative comparison for the Pure Shear test ($\ell_0 = 0.015$ mm). The 27×27 row is illustrative-reference only.

Method / Discretization	**Nodes / Elements**	h_s **[mm]**	h_s/ℓ_0	$P_{\max}$ **[kN]**	**Rel. Error (%)**	u_{crit} **[mm]**	**CPU [s]**
FEM (Miehe et al. [24])	30,000 Elem.	0.0035	0.23	441.5	Ref.	10.20×10^{-3}	310.8
MLPG (Shao et al. [30])	12,500 Nodes	0.0050	0.33	448.0	+1.47	10.35×10^{-3}	3,890.0
MLPG-RPIM (illustrative)	27×27 (729)	0.0385	2.57	476.2	+7.86	10.85×10^{-3}	54.1
MLPG-RPIM (Medium)	51×51 (2,601)	0.0200	1.33	452.1	+2.40	10.40×10^{-3}	395.2
MLPG-RPIM (Fine)	101×101 (10,201)	0.0100	0.67	443.8	+0.52	10.24×10^{-3}	3,460.0

Table 3 summarizes the quantitative comparison for the pure shear test. The 27×27 row is illustrative-reference only.

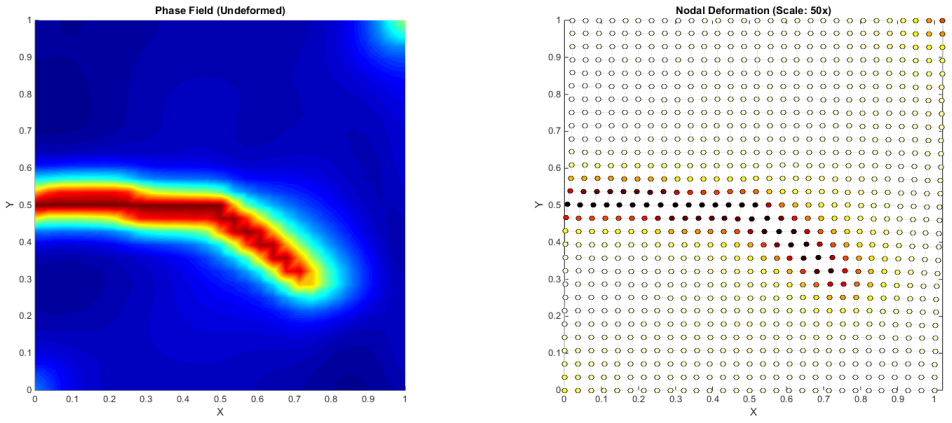


Figure 12: Pure shear at $t = 100$: (left) phase-field; (right) deformation (illustrative, 27×27)

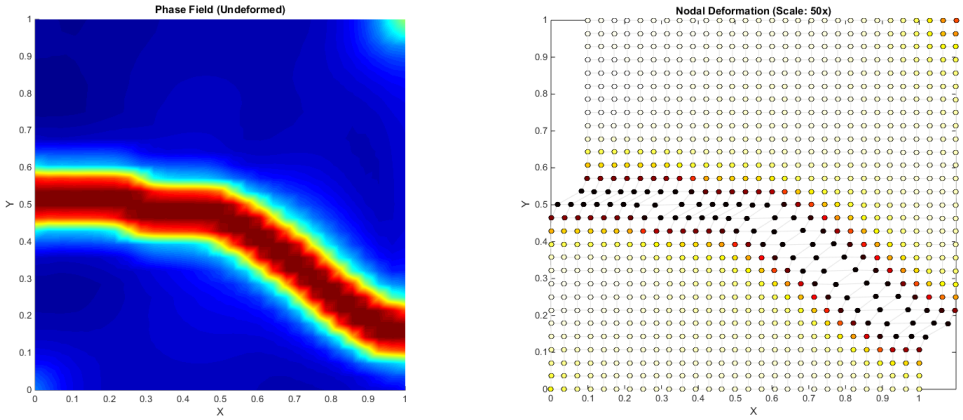


Figure 13: Pure shear at $t = 200$: (left) phase-field; (right) deformation (illustrative, 27×27)

5.4 Three-point bending benchmark

Symmetric and asymmetric beam configurations are evaluated; the asymmetric case is shown. Plane strain ($\varepsilon_{zz} = 0$). The crack initiates at the offset notch and propagates along a curvilinear path towards the loading point (Figures 15–18, all on the 27×27 grid, illustrative).

Table 4 presents the quantitative results for the Three-Point Bending test. The coarse $h_s = 1.0$ mm row is included for reference only; it is not used for any quantitative claim. The $h_s = 0.5$ and $h_s = 0.25$ mm rows are the quantitative entries.

5.5 Discussion on computational efficiency

The CPU times reported in Tables 2–4 are implementation-specific reference values and are not intended as a uniform performance benchmark. Because the MLPG-RPIM runs and the reference FEM/XFEM runs differ in degrees of freedom, quadrature density, and solver tolerances, no single cost ratio is

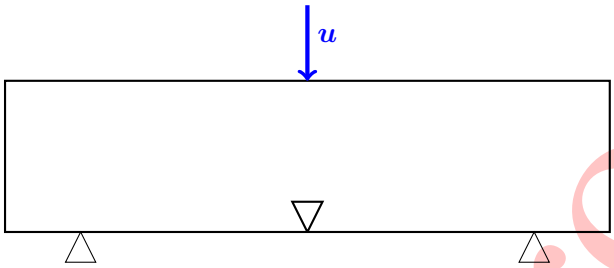


Figure 14: Boundary conditions for the Three-Point Bending benchmark

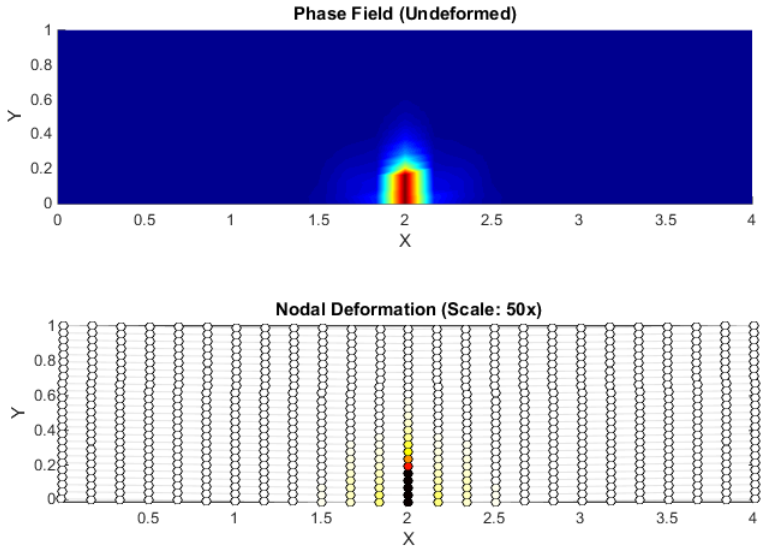


Figure 15: TPB at $t = 0$ (illustrative, 27×27 grid): the pre-crack is represented by the dual initialization of Section 4.4, namely $d = 1$ on the crack-line nodes together with the history initialization (36)

claimed. For the specific pair listed in Table 2 (101×101 MLPG-RPIM with 20,402 DOF versus the 30,000-element FEM reference with 60,000 DOF), the wall-clock times can be compared directly from the table; the MLPG-RPIM overhead originates from (i) the local moment-matrix inversion at each quadrature point ($N_s \approx 16$–25) and (ii) the higher-order quadrature (4×4 and 6×6) over overlapping support domains. The primary merit of the formulation remains its meshfree approximation and connectivity, which alleviate mesh distortion, remeshing, and pathological mesh-alignment dependence during arbitrary crack propagation.

6 Concluding remarks

This research has introduced an integrated phase-field fracture model using a meshless MLPG strategy. The field approximation and nodal connectivity are meshfree; Cartesian background cells are used solely for numerical integration and do not constitute a field-approximation mesh or a global element connectivity. The formulation combines the spectral strain decomposition of Miehe-type with RPIM shape func-

Correct Proof

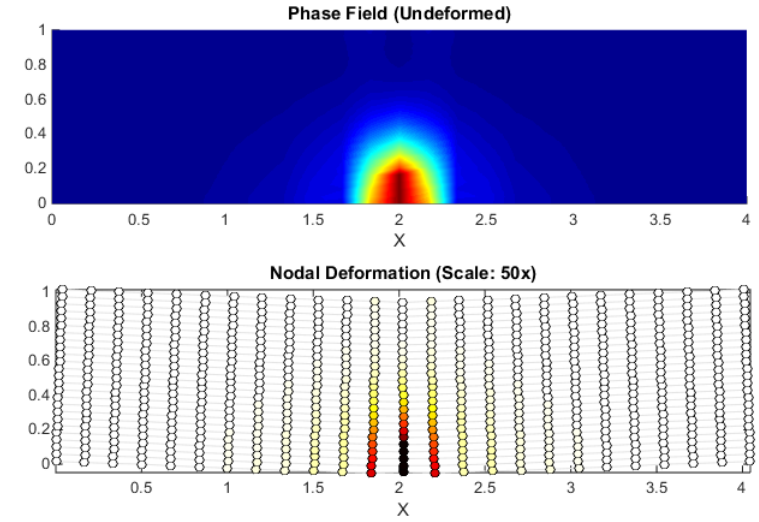


Figure 16: TPB at $t = 50$ (illustrative, 27×27)

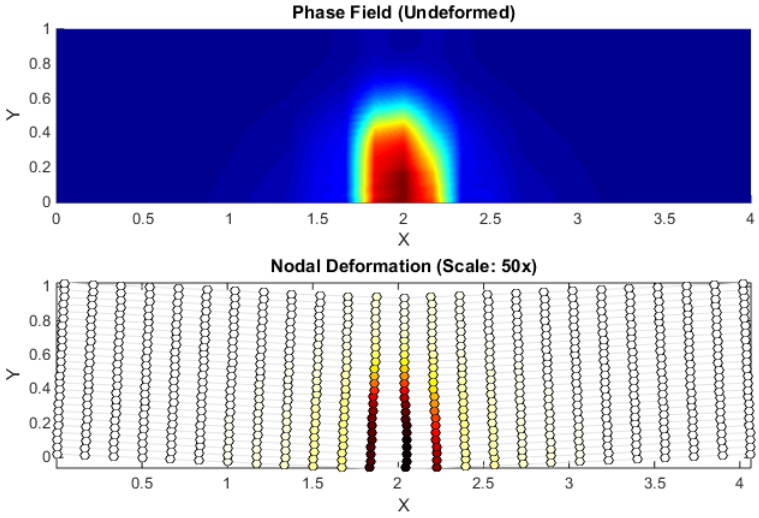


Figure 17: TPB at $t = 100$ (illustrative, 27×27)

tions possessing the Kronecker delta property, and employs a staggered solution scheme with a monotone history field to enforce damage irreversibility. The formulation is capable of capturing phenomena such as crack branching and coalescence, which are consistent with previously reported phase-field studies in rock-like materials [36, 37].

The numerical study is deliberately scoped: the 27×27 grid is used only for illustrative crack-path figures, while quantitative results are reported for the 51×51 and 101×101 grids, with the ratio h_s/ℓ_0 stated explicitly. The results show a consistent convergence trend toward the reference FEM/XFEM solutions as h_s decreases. The strict resolution requirement $h_s \leq \ell_0/2$ is treated as a conservative guideline;

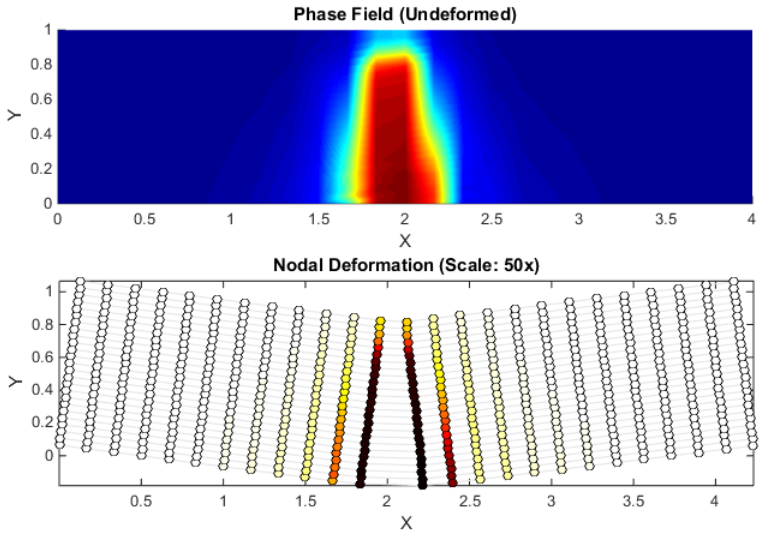


Figure 18: TPB at $t = 200$ (illustrative, 27×27)

Table 4: Quantitative comparison for the Three-Point Bending benchmark with eccentric notch. Coarse row is illustrative-reference only.

Method / Discretization	**Resolution**	h_s/ℓ_0	$P_{\max}$ **[kN]**	**Rel. Error (%)**	**Deflection at** $P_{\max}$ **[mm]**	**CPU [s]**
Experimental (Bittencourt [8])	—	—	1.51	—	0.065	—
FEM Phase-Field (Ambati et al. [2])	28,400 Elem.	—	1.54	+1.98	0.064	412.0
MLPG-RPIM (illustrative: $h_s = 1.0$ mm)	1,450 nodes	66.7	1.68	+11.25	0.069	115.4
MLPG-RPIM (Medium: $h_s = 0.5$ mm)	5,200 nodes	33.3	1.58	+4.63	0.066	780.0
MLPG-RPIM (Fine: $h_s = 0.25$ mm)	18,600 nodes	16.7	1.53	+1.32	0.064	4,680.0

a systematic study satisfying this criterion, together with curve-based error measures and a quantitative crack-path metric, is left for future work.

Acknowledgment

The authors thank the anonymous reviewers for their constructive comments, and the first author thanks Prof. Dr. Thomas Wick for insightful discussions on phase-field fracture modeling.

Conflict of interest

The author declares no conflict of interest.

References

[1] M. Abbaszadeh, M. Golmohammadi, M. Dehghan, *Simulation of activator–inhibitor dynamics based on cross-diffusion Brusselator reaction-diffusion system via a differential quadrature-radial*

Corrected Proof

point interpolation method (DQ-RPIM) technique, Eur. Phys. J. Plus, **136** (2021) Article No. 59.

[2] M. Ambati, T. Gerasimov, L. De Lorenzis, *A review on phase-field models of brittle fracture and a new fast hybrid formulation*, Comput. Mech. **55** (2015) 383–405.

[3] F. Amiri, D. Millán, M. Arroyo, M. Silani, T. Rabczuk, *Fourth order phase-field model for local max-ent approximants applied to crack propagation*, Comput. Methods Appl. Mech. Eng. **312** (2016) 254–275.

[4] H. Amor, J.-J. Marigo, C. Maurini, *Regularized formulation of the variational brittle fracture with unilateral contact: Numerical experiments*, J. Mech. Phys. Solids **57** (2009) 1209–1229.

[5] S.N. Atluri, *The Meshless Local Petrov–Galerkin (MLPG) Method for Domain and BIE Discretizations*, Tech Science Press, 2004.

[6] S.N. Atluri, T. Zhu, *A new meshless local Petrov–Galerkin (MLPG) approach in computational mechanics*, Comput. Mech. **22** (1998) 117–127.

[7] T. Belytschko, Y.Y. Lu, L. Gu, *Element-free Galerkin methods*, Int. J. Numer. Methods Eng. **37** (1994) 229–256.

[8] T.N. Bittencourt, P.A. Wawrzynek, A.R. Ingraffea, J.L. Sousa, *Quasi-automatic simulation of crack propagation for 2D LEFM problems*, Eng. Fract. Mech. **55** (1996) 321–334.

[9] B. Bourdin, G.A. Francfort, J.-J. Marigo, *Numerical experiments in revisited brittle fracture*, J. Mech. Phys. Solids **48** (2000) 797–826.

[10] B. Bourdin, G.A. Francfort, J.-J. Marigo, *The variational approach to fracture*, J. Elast. **91** (2008) 5–148.

[11] S. Das, T.I. Eldho, *A coupled flow and transport model for simulation of multi-species reactive transport in unconfined aquifer using meshless local Petrov–Galerkin (MLPG) method*, Environ. Sci. Pollut. Res. **30** (2023) 105556–105574.

[12] G.A. Francfort, J.-J. Marigo, *Revisiting brittle fracture as an energy minimization problem*, J. Mech. Phys. Solids **46** (1998) 1319–1342.

[13] E. Gholamipour, A. Shirzadi, H. Hosseinzadeh, V. Sladek, J. Sladek, *Mathematical relationships and novel extensions of MLPG variants*, Comput. Math. Appl. **205** (2026) 212–228.

[14] A.A. Griffith, *The phenomena of rupture and flow in solids*, Philos. Trans. R. Soc. A **221** (1921) 163–198.

[15] Y.T. Gu, *Meshfree Methods and Their Applications*, Springer, 2011.

[16] T. Guo, O. Nikan, W. Qiu, D. Xu, *Localized meshless approaches based on theta method and BDF2 for nonlinear Sobolev equation arising from fluid dynamics*, Commun. Nonlinear Sci. Numer. Simul. **117** (2023) 106989.

Corrected Proof

[17] S. Nesari Haghighi Fard, M. Najafi, V. Enjilela, A. Imam, A. Karimipour, *Application extension of the meshless local Petrov–Galerkin method: Non-Newtonian fluid flow implementations*, Eng. Anal. Bound. Elem. **156** (2023) 321–343.

[18] B. Hooshyarfarzin, M. Abbaszadeh, M. Dehghan, *Simulation of coupled elasticity problem with pressure equation: hydroelastic equation*, Multidiscip. Model. Mater. Struct. **20** (2024) 577–616.

[19] G.R. Irwin, *Analysis of stresses and strains near the end of a crack traversing a plate*, J. Appl. Mech. **24** (1957) 361–364.

[20] S.L. Li, K.Y. Liu, S.Y. Long, G.Y. Li, *The natural neighbour Petrov–Galerkin method for thick plates*, Eng. Anal. Bound. Elem. **35** (2011) 616–622.

[21] W.K. Liu, S. Jun, Y.F. Zhang, *Reproducing kernel particle methods*, Int. J. Numer. Methods Fluids **20** (1995) 1081–1106.

[22] G.R. Liu, Y.T. Gu, *An Introduction to Meshfree Methods and Their Programming*, Springer, 2005.

[23] T.K. Mandal, V.P. Nguyen, A. Heidarpour, *Phase field and gradient enhanced damage models for quasi-brittle failure: A numerical comparative study*, Eng. Fract. Mech. **207** (2019) 48–67.

[24] C. Miehe, M. Hofacker, F. Welschinger, *A phase field model for rate-independent crack propagation: Robust algorithmic implementation based on operator splits*, Comput. Methods Appl. Mech. Eng. **199** (2010) 2765–2778.

[25] C. Miehe, F. Welschinger, M. Hofacker, *Thermodynamically consistent phase-field models of fracture: Variational principles and multi-field FE implementations*, Int. J. Numer. Methods Eng. **83** (2010) 1273–1311.

[26] N. Moës, J. Dolbow, T. Belytschko, *A finite element method for crack growth without remeshing*, Int. J. Numer. Methods Eng. **46** (1999) 131–150.

[27] T.T. Nguyen, J. Yvonnet, Q.-Z. Zhu, M. Bornert, C. Chateau, *A phase field method to simulate crack nucleation and propagation in strongly heterogeneous materials*, Eng. Fract. Mech. **139** (2015) 18–39.

[28] O. Nikan, Z. Avazzadeh, J.A. Tenreiro Machado, *Numerical treatment of microscale heat transfer processes arising in thin films of metals*, Int. Commun. Heat Mass Transf. **132** (2022) 105892.

[29] J.R. Rice, *A path independent integral and the approximate analysis of strain concentration by notches and cracks*, J. Appl. Mech. **35** (1968) 379–386.

[30] Y. Shao, Q. Duan, S. Qiu, *Adaptive consistent element-free Galerkin method for phase-field model of brittle fracture*, Comput. Mech. **64** (2019) 1121–1139.

[31] A. Shafiei, S.M. Mosavi Nezhad, *An adaptive multi-resolution framework for the meshless local Petrov–Galerkin method*, Comput. Mech. (2025).

[32] J.G. Wang, G.R. Liu, *A point interpolation meshless method based on radial basis functions*, Int. J. Numer. Methods Eng. **54** (2002) 1623–1648.

Corrected Proof

[33] T. Wick, *Multiphysics Phase-Field Fracture: Modeling, Adaptive Discretizations, and Solvers*, De Gruyter, 2020.

[34] J.-Y. Wu, *A unified phase-field theory for the mechanics of damage and quasi-brittle failure*, J. Mech. Phys. Solids **103** (2017) 72–99.

[35] S.-W. Yang, P.R. Budarapu, D.R. Mahapatra, S.P.A. Bordas, G. Zi, T. Rabczuk, *A meshless adaptive multiscale method for fracture*, Comput. Mater. Sci. **96** (2015) 382–395.

[36] S. Zhou, T. Rabczuk, X. Zhuang, *Phase field modeling of crack propagation, branching and coalescence in rocks*, Adv. Eng. Softw. **122** (2018) 31–49.

[37] X. Zhou, L. Wang, Y. Shou, *Understanding the fracture mechanism of ring Brazilian disc specimens by the phase field method*, Int. J. Fract. **226** (2020) 17–43.

[38] T. Zhu, S.N. Atluri, *A modified collocation method and a penalty formulation for enforcing the essential boundary conditions in the element-free Galerkin method*, Comput. Mech. **21** (1998) 211–222.

Corrected Proof